International Journal of Coal Geology 238 (2021) 103729

Contents lists available at ScienceDirect

International Journal of Coal Geology

journal homepage: www.elsevier.com/locate/coal

An insight into quartz mineral interactions with kerogen in Green River oil shale

H.M. Nasrullah Faisal, Kalpana S. Katti, Dinesh R. Katti *

Department of Civil and Environmental Engineering, North Dakota State University, Fargo, ND 58105, USA

ARTICLE INFO

Keywords:
Oil shale
Kerogen
Quartz
Molecular dynamics
Molecular interactions

ABSTRACT

Green River oil shale is an organic-inorganic macromolecular composite system. Identifying the interactions between nanoscale organic kerogen and the inorganic mineral matrix in oil shale is an important step towards the design of technologies for economic and efficient recovery of shale oil. Quartz (SiO_2), one of the tectosilicate minerals present in the Green River oil shale, is modeled to determine the interactions with the 3D kerogen model. The molecular dynamics simulation technique is used as the tool for modeling the interactions. Two models with different orientations of quartz mineral and kerogen are built to evaluate the role of mineral orientation on the molecular interactions. The models are simulated at room temperature and pressure (300 K and 1.013 bar). The kerogen-quartz interactions are evaluated with respect to eight kerogen fragments. We observe that different fragments within the 3D Kerogen molecules interact with the quartz depending upon the quartz orientation. In both cases, the unconstrained ammonium (NH_4) ions from the adjacent layer of kerogen migrate to the quartz cavities. All the non-interacting kerogen fragments move away from quartz. The nonbonded interactions between kerogen and quartz are generally electrostatic. The presence of quartz mineral also affects the inter-fragment and inter-layer interactions within the kerogen molecule.

1. Introduction

Modern civilization heavily depends on the consumption of energy. The search for 'energy sources' has been one of the most major concerns of humanity for the last two centuries. Crude oil, a critical source of energy, has been in great demand globally. The limited availability of crude oil resources has led the researchers to find newer sources of petroleum. Oil shale is being considered as a potential alternative to traditional petroleum resources (crude oil, coal, gas) (Deng et al., 2011). Oil shales have been discovered in 27 countries, and some of them have begun extracting shale oil (Alstadt et al., 2012). Green River formation in Utah, Wyoming, and Colorado is the largest deposit of oil shale in the world (Guo et al., 2014). This deposit is estimated to be a resource of 1.5 trillion barrels of shale oil, including a reserve of 800 billion barrels (Taskforce on Strategic Unconventional Fuels, 2007).

Oil shale is a dense, fine-grained, laminated sedimentary rock that contains both organic and inorganic materials, and the organic material is considered to be trapped in the inorganic matrix (Karabakan and Yurum, 1998). The organic material is mainly kerogen with small amounts of bitumen, while the inorganic components are minerals. The minerals present are typically carbonates, silicates, and pyrites (Yan et al., 2013). Kerogen is the material of interest in oil shale as the thermal cracking of kerogen yields shale oil. Kerogen is a high molecular weight insoluble organic heteropolymer of carbon, oxygen, hydrogen, nitrogen, and sulfur. It has been classified into Type I, Type II, and Type III depending upon its hydrogen to carbon ratio and oxygen to carbon ratio (Razvigorova et al., 2008). Green River oil shale contains 11.04% Type I kerogen, 2.76% bitumen, and 86.2% mineral by weight (Cane, 1976). Both carbonate and silicate minerals constitute almost half of the mineral matter, while pyrite exists in small amounts.

Early research proved that the presence of the mineral matrix with kerogen affects the qualitative and quantitative distribution of hydrocarbons in the pyrolysis process (Eglinton et al., 1986). However, researchers have different opinions regarding kerogen-mineral interactions during pyrolysis. Some TG analyses revealed that all minerals inhibit the decomposition of kerogen during pyrolysis (Aboulkas and El Harfi, 2008, 2009). On the other hand, other TG analyses showed that montmorillonite clay minerals offer catalytic effect on the decomposition of oil shale (Borrego et al., 2000). Several experiments demonstrated that the removal of carbonate minerals decreased the

* Corresponding author.
E-mail address: Dinesh.Katti@ndsu.edu (D.R. Katti).

https://doi.org/10.1016/j.coal.2021.103729
Received 3 December 2020; Received in revised form 12 March 2021; Accepted 13 March 2021
Available online 16 March 2021

hydrocarbon yield while the removal of silicate minerals increased the hydrocarbon yield (Ballice, 2005; Sert et al., 2009). Some researchers also hypothesized that the effect of mineral matrix on kerogen primarily depends upon the oil shale mineral composition (Pan et al., 2016). If the carbonates make up the greater portion of minerals, they have a catalytic effect on oil shale pyrolysis. However, if the silicates are predominantly present in oil shale, they exhibit an inhibitory effect on kerogen pyrolysis. Nevertheless, as the Green River oil shale contains carbonates and silicates in equal percentage (by weight), their impact on pyrolysis is still unclear.

Our research group has carried out extensive investigations on kerogen mineral interactions in the Green River oil shale. We determined that kerogen exists in pockets of the order of 10s of nm in Green River oil shale, and kerogen-mineral interactions are primarily nonbonded (Alstadt et al., 2012; Alstadt et al., 2016). Our previous studies have shown that nanoscale coexistence of minerals and organics affects the behavior of organic macromolecules in seashells (Ghosh et al., 2007), polymer clay nanocomposites (Faisal et al., 2021; Sikdar et al., 2008), human bone (Bhowmik et al., 2009a), and polymer hydroxyapatite nanocomposites (Bhowmik et al., 2009b) mainly because of nonbonded interactions. Solid rock oil shale can be converted into liquid shale oil by pyrolysis procedure (Ballice, 2006). Different physical and chemical methods are utilized to isolate the organic kerogen from the inorganic mineral matters (Vandenbroucke and Largeau, 2007). Critical point drying, gravity flotation, subcritical water extraction and inorganic acid leaching are the most commonly employed techniques (Forsman and Hunt, 1958; Luong et al., 2015; Saxby, 1970; Stankiewicz et al., 1996; Suleimenova et al., 2014). The effective application of all these procedures is potentially hindered by the lack of detailed understanding of the interactions between the organic kerogen and inorganic minerals (Liu et al., 2019). Moreover, the quality and yield of crude oil is also dependent upon the organic-inorganic interactions of oil shale (Borrego et al., 2000; Pan et al., 2016). Therefore, it is essential to investigate the interactions between the organic kerogen and inorganic minerals to extract the trapped kerogen from the mineral matrix. Different experimental studies investigated the organic-inorganic interactions within the oil shale. Supercritical ethanolysis (SE) and stepwise acid treatment of oil shale revealed that carbonate minerals primarily interact with carboxylic acids while silicate minerals form Si—O ether bonds (Liu et al., 2019). Liquid chromatography fractionation and Fourier transform infrared spectroscopy of oil shale also showed the similar results (Chang et al., 2017). However, these experimental techniques can investigate the interactions for a category of minerals (calcites/silicates etc.) instead of determining the interactions of individual mineral (calcite, dolomite, clay, quartz etc.) with organic kerogen. In-silico investigation of kerogen-mineral interactions through molecular dynamics simulations can be an efficient alternative solution towards this problem. Our research group has been working to devise a computational testbed to model the interactions of organic kerogen with the mineral matrix. As the organic kerogen is trapped inside the mineral matrix in Green River oil shale, the ultimate goal is to model the kerogen in the proximity of all the present minerals through molecular dynamics simulations. Before modeling the kerogen with all minerals, it would be beneficial to model kerogen with each of the individual mineral to identify the interactions that take place between kerogen and only that mineral. Inspecting the interactions of kerogen with individual mineral will help us to identify the major interacting minerals within the oil shale. This virtual screening of interacting minerals of oil shale will help to model kerogen-mineral matrix interactions in a more efficient manner by considering only the significantly interacting minerals. Different research groups have undertaken the computational approaches to investigate the kerogen-mineral interactions (Hantal et al., 2014; Zhang et al., 2020). The previous studies from our group determined the interactions of kerogen with montmorillonite and calcite mineral (Faisal et al., 2020; Katti et al., 2017). For the development of robust testbeds for kerogen interactions with all major Green River Oil Shale minerals, in this study we investigate the molecular interactions of kerogen with quartz mineral using molecular dynamics simulations.

Molecular dynamics (MD) simulation predicts the time-dependent behavior of a molecular system. The energy of the system is computed using molecular mechanics calculations. At first, we performed MD simulations of three kerogen moieties (pyridine, quinaldine, and heptylamine) with Na-montmorillonite clay and verified the findings of MD simulations by performing XRD and FTIR experiments (Katti et al., 2014). We then constructed a complete 3D kerogen model (12-unit kerogen) and simulated it with Na-montmorillonite clay, which revealed significant nonbonded interactions between clay and kerogen (Katti et al., 2017). Molecular interactions between organic kerogen and carbonate mineral (calcite) have been investigated in terms of energy and conformations (Faisal et al., 2020).

Quartz (SiO_2) is the most commonly found silicate mineral on earth. It makes up about one-fifth of the earth's exposed crust (Skelton et al., 2011). Apart from Na-montmorillonite clay, quartz is another major silicate mineral of Green River oil shale. It makes up about 8.6% of the Green River oil shale (Cane, 1976) and can have significant interactions with kerogen. Quantum chemical calculations have been used to explore the interactions between kerogen (type II) and silica in gas shale (Hantal et al., 2014). A model of CS1000 (a disordered porous 3D carbon structure lacking oxygen) (Jain et al., 2006; Pikunic et al., 2003) was used as type II kerogen to reconstruct interface with α-cristobalite. However, Green River oil shale contains type I kerogen, unlike the gas shale. In this study, we present the results of molecular dynamics simulations of quartz mineral with type I kerogen to understand their interactions in the Green River oil shale. This study primarily seeks to develop a computational test-bed for investigating the molecular interactions between the organic constituent (Type I kerogen) of Green River oil shale and inorganic quartz mineral in a laboratory environment i.e. Normal Temperature and Pressure conditions.

2. Methodology

2.1. Model construction

Quartz is a trigonal crystal system. It belongs to the tectosilicate group that exhibits a complex 3-dimensional framework. The silica (SiO_4) tetrahedron is the principal building block of the 3D frame. These silica tetrahedrons build large framework structure by sharing corner oxygen atoms. Due to this behavior, the corner oxygen atoms are also termed as bridging oxygen atoms. The three-fold screw axis (3_2) is observed in the quartz framework. The quartz structure consists of holes or cavities, usually termed as stuffing sites. Different alkaline earth elements or groups can occupy these sites. In nature, quartz can occur in four different polymorphs (α, β, tridymite, and cristobalite) depending upon its surrounding environment. The α-quartz predominantly occurs at normal temperature and pressure while three other polymorphs usually occur at high temperature and pressure conditions. As we are mainly focused on determining the interactions between quartz mineral and kerogen at NTP condition (300 K and 1 bar), we built the crystal structure of α-quartz. The space group of α-quartz is $P3_221$ (No. 154). The unit cell dimensions of alpha-quartz are a = b = 4.9134 Å, c = 5.4052 Å, and $\alpha = \beta = 90^\circ$, $\Upsilon = 120^\circ$ (Le Page and Donnay, 1976). Using this information and fractional coordinates of atoms, the unit cell of α-quartz is constructed using Materials Studio 7.0 (Fig. 1a, b). We then performed 'X-ray Powder Diffraction' on our constructed quartz unit cell model using the 'Reflex' module of Materials Studio 7.0. The resultant diffraction peaks (Fig. 2a) are in exact accordance with the diffraction peaks of the quartz sample found in rocks (Antao et al., 2008; Ikuta et al., 2007). The matching of the diffraction pattern is performed by MATCH! 3.7.0 Software. This exercise validates our constructed quartz unit cell model. For determining the interactions with the 12-unit 3D kerogen model, we have built a quartz supercell by repeating the quartz unit cell. The dimensions of the quartz supercell are 14.54 Å × 83.51 Å × 10.80 Å.

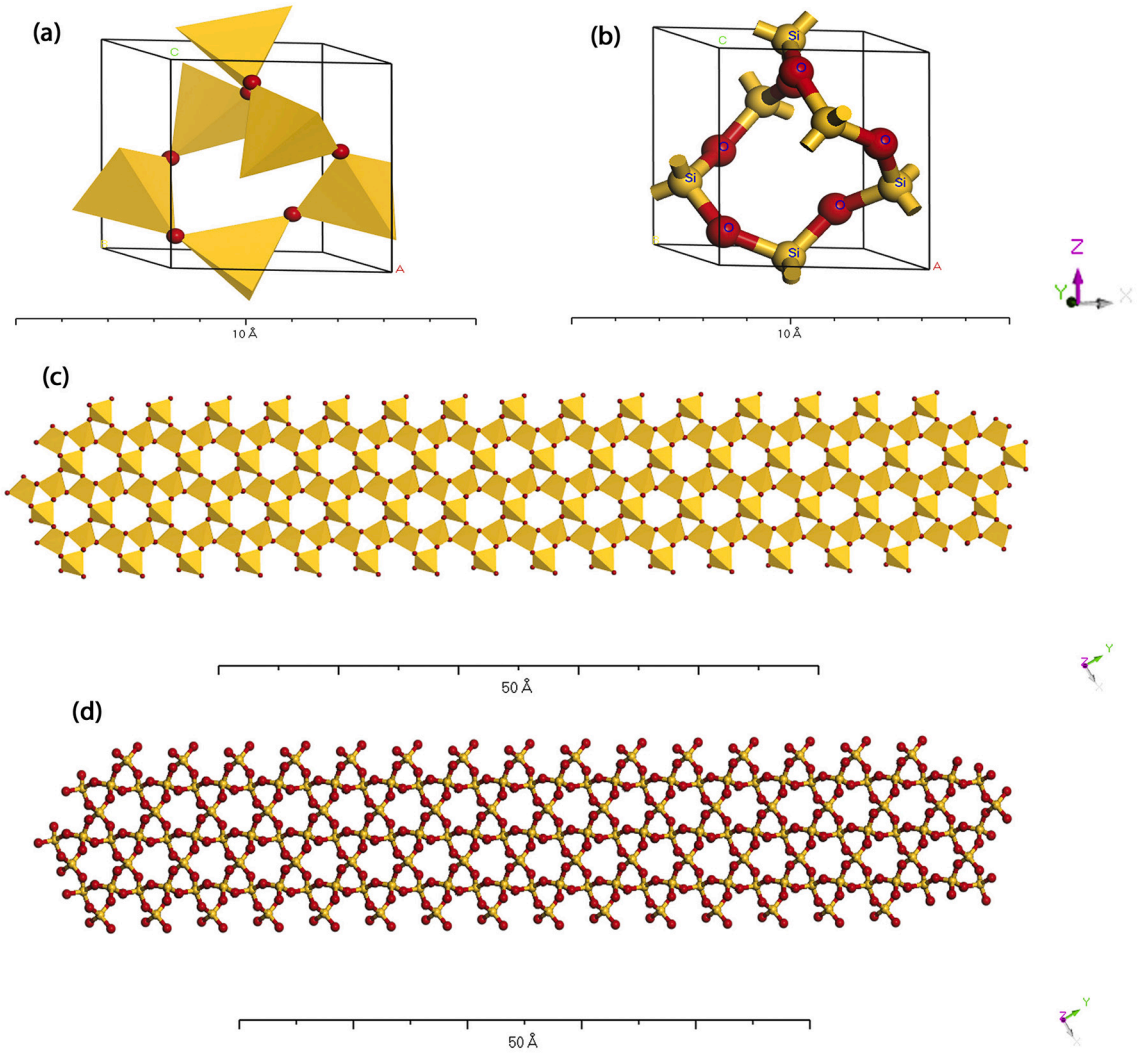

Fig. 1. Molecular structure of a unit cell of α-quartz (a) polyhedron view, (b) ball and stick view with a label on atoms, and quartz supercell (c) polyhedron view, (d) ball and stick view. All the representations were generated by Materials Studio 7.0.

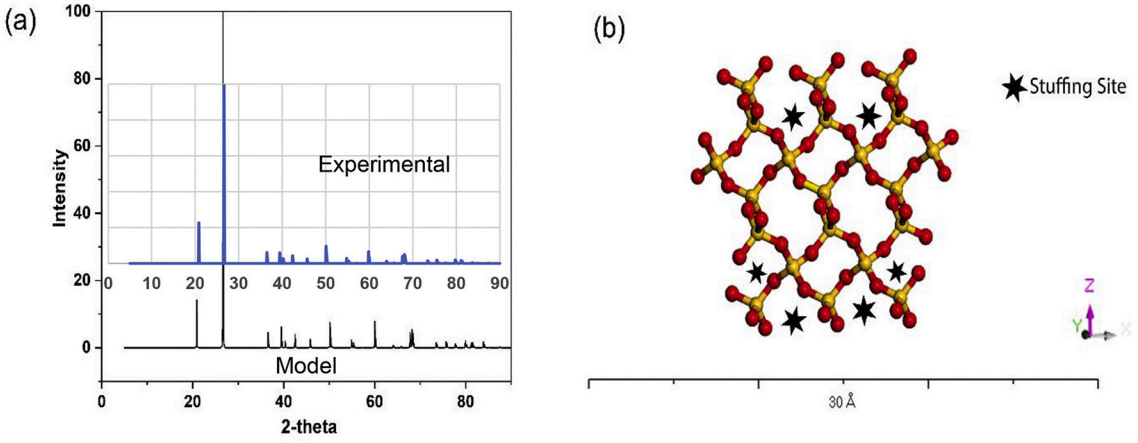

Fig. 2. (a) The XRD spectrum of constructed α-quartz unit cell model with the experimental spectrum (reproduced from Ikuta et al., 2007) on it, (b) Stuffing sites (cavities) of quartz supercell.

This model contains 1197 atoms in total. In this supercell, the silica tetrahedrons are arranged in such a way to exhibit a three-fold screw axis (Fig. 1c, d) and stuffing sites (Fig. 2b). The quartz supercell was also constructed by using Materials Studio 7.0.

The 3D kerogen model of Green River oil shale used in this study has been developed, homogenized through stepwise annealing and validated in our prior work (Katti et al., 2017). The construction of the 3D kerogen model was based on Siskin's 2D kerogen model (Orendt et al., 2013; Siskin et al., 1995). Siskin generated the type I kerogen model using nondestructive chemical derivatization and characterization via NMR and mass spectroscopy. This structure was later validated against the NMR, XPS (X-ray photoemission spectroscopy), and sulfur XANES (X-ray absorption near edge structure) data (Kelemen and Siskin, 2004). The chemical formula of the kerogen unit is $C_{645}H_{1017}N_{19}O_{17}S_4$. For the convenience of structure building and parametrization the kerogen unit was considered to be made up (agglomerate) of seven different hydrocarbon fragments and four independent ammonium (NH_4) groups associated with the fragments. In the present study, these seven hydrocarbon fragments will be termed as fragment 1 through fragment 7. The independent ammonium ions are considered as fragment 8. The model building procedure was described in details in one of the earlier studies from our group (Katti et al., 2017). At first, all the kerogen fragments were built using Materials Studio 7.0. Then all the fragments were merged into unit kerogen model using the VMD 1.9.3. This unit kerogen model was parameterized using the CHARMm General Force Field (CGenFF) which assigns the atom types and partial charges in a rule-based automated manner. In order to mimic the tens of nanometer sized kerogen pockets, 12 units of kerogen were merged using the VMD. The geologic pressure condition was modeled by applying the in-situ stresses on the 12-unit kerogen model. A series of molecular dynamics simulations were performed on the kerogen model to obtain the equilibrated conformation that will be used for determining the interactions with minerals. At the beginning, minimization was performed on the model at 0 K and 0 bar conditions to remove the artifacts from the model. Then simulated annealing was performed by gradually increasing and decreasing the temperature of the 12-unit kerogen model in a stepwise process for achieving an optimized conformation. The temperature was increased from 0 K to 500 K and then decreased to 300 K while the pressure was increased from 0 bar to 1.01325 bar. At last, the model was equilibrated at NTP condition (300 K and 1.01325 bar) for 5 ns. Radial pair distribution function (RPDF) were calculated for the equilibrated 12-unit kerogen model to validate against the previously reported NMR data (Orendt et al., 2013). The different stages of model building and validation are shown in consecutive figures of the Supplementary material (Supplementary figs. 4–9). Each kerogen unit contains four independent ammonium (NH_4) groups associated with the seven hydrocarbon fragments. In the present study, these seven hydrocarbon fragments will be termed as fragment 1 through fragment 7. Therefore the 12-unit kerogen model consists of 12 segments of each fragment. For the convenience of energy analysis, we will reference all the independent ammonium groups as fragment 8.

Table 1 shows the chemical composition of kerogen fragments. The detailed description of kerogen fragments is provided in the previous study (Katti et al., 2017). The 12 kerogen units are identified as top and bottom chains (layers) along the *Z*-axis. Thus, each chain has six kerogen units, i.e., 30 NH_4 groups in total. The dimensions of the 12-unit kerogen model are 71.92 Å × 88.98 Å × 63.89 Å (Fig. 3a, b).

Table 1
Chemical composition of kerogen fragments (Katti et al., 2017).

Kerogen fragment	Chemical formula
1	$C_{18}H_{38}$
2	$C_{18}H_{30}$
3	$C_{20}H_{42}$
4	$C_{45}H_{60}O$
5	$C_{75}H_{117}N_4O_5$
6	$C_{102}H_{167}NOS_2$
7	$C_{367}H_{547}N_{10}O_{10}S_2$
8	NH_4

The 12-unit kerogen and quartz supercell structures were merged using the "Merge Structures" plugin of Visual Molecular Dynamics (VMD) 1.9.3.

The merging of structures was performed in two different ways to build two different models. In the first model, the quartz supercell is placed on top of the 12-unit kerogen (Fig. 3c), while in the second model, quartz supercell is placed at the bottom of kerogen along the Z-axis (Fig. 3d). The two models allow for evaluating the interactions between the kerogen and quartz for two potential quartz orientations with respect to kerogen. We have not incorporated silanol (SiOH) groups in the model as the previous FTIR study of Green River oil shale did not show the presence of explicit water (Alstadt et al., 2012). A cutoff distance of 16 Å has been employed for computing local non-bonded interactions. In order to be consistent with NAMD periodic boundary algorithms, the periodic boundary conditions have been made sufficiently large so that the quartz supercell can not see the organic kerogen from both sides. Therefore, all the resultant non-bonded interactions originated inside the periodic box rather than across the periodic boxes.

2.2. Model parameterization

The quartz model is parameterized using the CHARMm (Chemistry at HARvard Macromolecular Mechanics) force field (Vanommeslaeghe et al., 2010). It contains a set of functions and associated constants to define energy expression. CHARMm uses five energy terms, including one electrostatic term. The following equation describes the CHARMm force field:

$$E = E_{bond} + E_{angle} + E_{dihedral} + E_{VDW} + E_{electrostatic} \tag{1}$$

$$E = k_r(r - r_0)^2 + k_\theta(\theta - \theta_0)^2 + k_\varphi[1 + cos(n\varphi + \delta)] + \epsilon\left[\left(\frac{Rmin}{r}\right)^{12} - 2\left(\frac{Rmin}{r}\right)^{6}\right] + \frac{q_i q_j}{r_{ij}} \tag{2}$$

The first three terms of the right side of equations represent bonded energy, while the last two terms represent nonbonded energy. Here k_r, k_θ *and* $k\varphi$ express bond stretching, angle bending, and dihedral force constant, respectively. The equilibrium bond length, angle, dihedral and phase shift are symbolized by r_0, θ_0, φ *and* δ accordingly. Lennard-Jones VDW parameters are represented by ϵ and *Rmin*. The partial electrostatic atomic charge is represented by *q*,and the interatomic distance is expressed by *r*.The CHARMm force field parameters of α-quartz have been obtained from the literature where the authors proposed a common force field for all silica minerals (α-quartz, α-cristobalite, and amorphous silica) (Emami et al., 2014). They determined the structural, mechanical, and vibrational properties of these minerals utilizing the force field and cross-validated them with experimental results. The CHARMm force field parameters of 3D kerogen that were found in our previous study (Katti et al., 2017) have been utilized.

2.3. Simulation details

Molecular dynamics simulations of both models (quartz supercell on top of kerogen and quartz supercell at the bottom of kerogen along *Z*-axis) were performed using NAMD 2.12 (Phillips et al., 2005). NAMD was developed by the Theoretical and Computational Biophysics Group at the Beckman Institute for Advanced Science and Technology at the University of Illinois at Urbana-Champaign. Both models were minimized at zero Kelvin temperature (0 K) and 0 bar pressure using the conjugate gradient method (Payne et al., 1992). Next, both the models were brought to room temperature (300*K*) and pressure (1.0125 bar) in seven steps. First, the temperature was raised from 0 K to 300 K in three steps, and then the pressure was increased from 0 bar to 1.0125 bar in

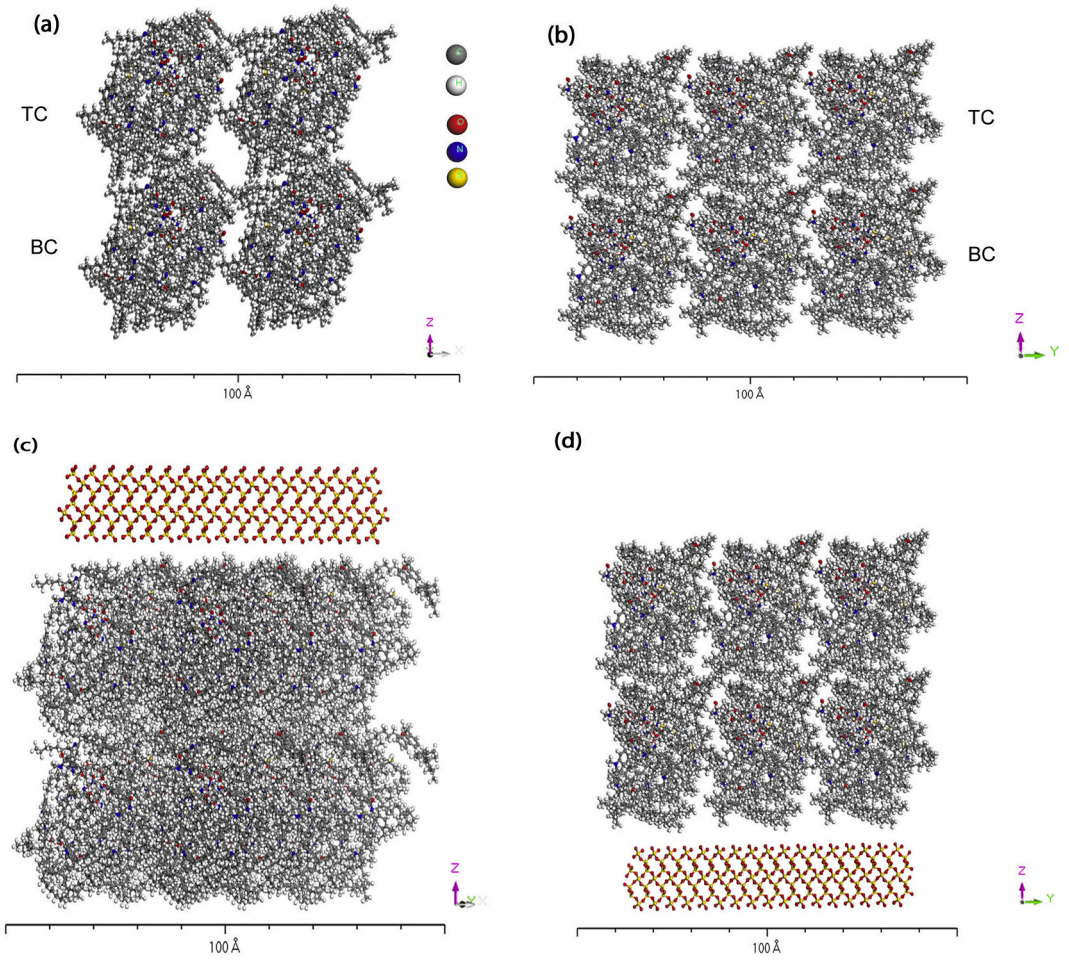

Fig. 3. Molecular models of (a, b) three-dimensional 12-unit kerogen, (c) quartz supercell on top of kerogen, and (d) quartz supercell at the bottom of kerogen. TC and BC represent the top and bottom chain (layer) of kerogen along the Z-axis, respectively. All the representations were generated by Materials Studio 7.0.

four steps. Both models were run at room temperature and pressure (isobaric-isothermal) for 4 ns with a time step of 0.5 fs (8,000,000 steps) as the models reached equilibrium condition within 4 ns. In both cases, the quartz supercell was constrained harmonically to maintain the crystallinity while kerogen was unconstrained. Harmonic constraints compel the atoms to remain in a reference position by applying harmonic force constants. Any movement from the reference position is penalized which restricts the large atomic motion of the constrained atoms. All the simulations were conducted at North Dakota State University Center for Computationally Assisted Science and Technology (CCAST). Each simulation utilized one node, dual socket Intel Xeon 2670v2 "Ivy Bridge" 2.5GHz with 64GB DDR3 RAM at 1866 MHz and 20 processors.

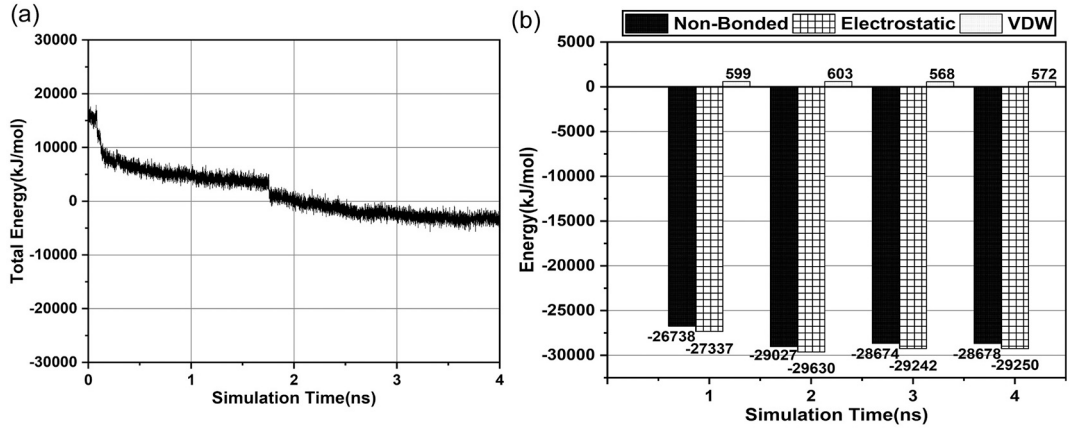

Fig. 4. (a) Total energy vs. time plot, and (b) bar graph showing nonbonded energy acting between quartz supercell and 12-unit kerogen with time for 'quartz supercell on top of kerogen' model.

3. Results and discussion

3.1. Quartz supercell on top of kerogen model

The total energy of MD simulation is the summation of potential (bonded & nonbonded) and kinetic energy. Fig. 4a illustrates that the total interaction energy between the quartz supercell and 12-unit kerogen has reached the equilibrium zone in less than 4 ns of the simulation period. Snapshots of the model were taken at 1 ns intervals to represent the conformations of quartz supercell on top of 12-unit kerogen (Fig. 5).

Immediately after the simulations were initiated at room temperature and pressure, 13 NH_4 groups among 24 from the top chain (layer) of kerogen moved to the quartz supercell. These NH_4 groups occupied the stuffing sites (holes) of quartz structure (Fig. 6a). All the fragments of kerogen except fragments 4 and 5 slowly moved away from the quartz supercell. At the end of 1 ns, four segments of fragment 4 and three segments of fragment 5 were in close proximity of the supercell (Fig. 5a). All of the interacting fragments belonged to the top chain (layer) of kerogen. The sudden decrease in total energy around 1.7 ns (Fig. 4a) indicated the separation of bottom kerogen layer from the top kerogen layer. After the simulation period of 2 ns, a total of 14 NH_4 groups from the top chain moved to the supercell while other NH_4 groups moved towards the bottom chain of kerogen. Four segments of fragment 4 were still in the close proximity of the quartz. But instead of three, only one segment of fragment 5 had interaction with supercell, which implies that most of the fragments of kerogen were further moving away from quartz (Fig. 5b and Supplementary Fig. 15). At the end of 3 ns, all the fragments of kerogen except the ones close to the quartz supercell finally moved beyond the cutoff distance (Fig. 5c). The top chain of kerogen merged into the bottom chain at that point.

This action increased the interactions between the kerogen chains (layers). As the kerogen fragments did not change their conformations from 3 ns to 4 ns, the simulation is considered to reach the equilibrium zone at 4 ns (Fig. 5d).

The nonbonded interaction energy is the summation of electrostatic and Van der Waals (VDW) energy. From Table 2, it is evident that only the fragments 4, 5, and 8 (NH_4 groups) of 12-unit kerogen interacted with the quartz supercell. Fragments 6 and 7 had very little interaction with the quartz. Approximately 95% of the total attractive interactions

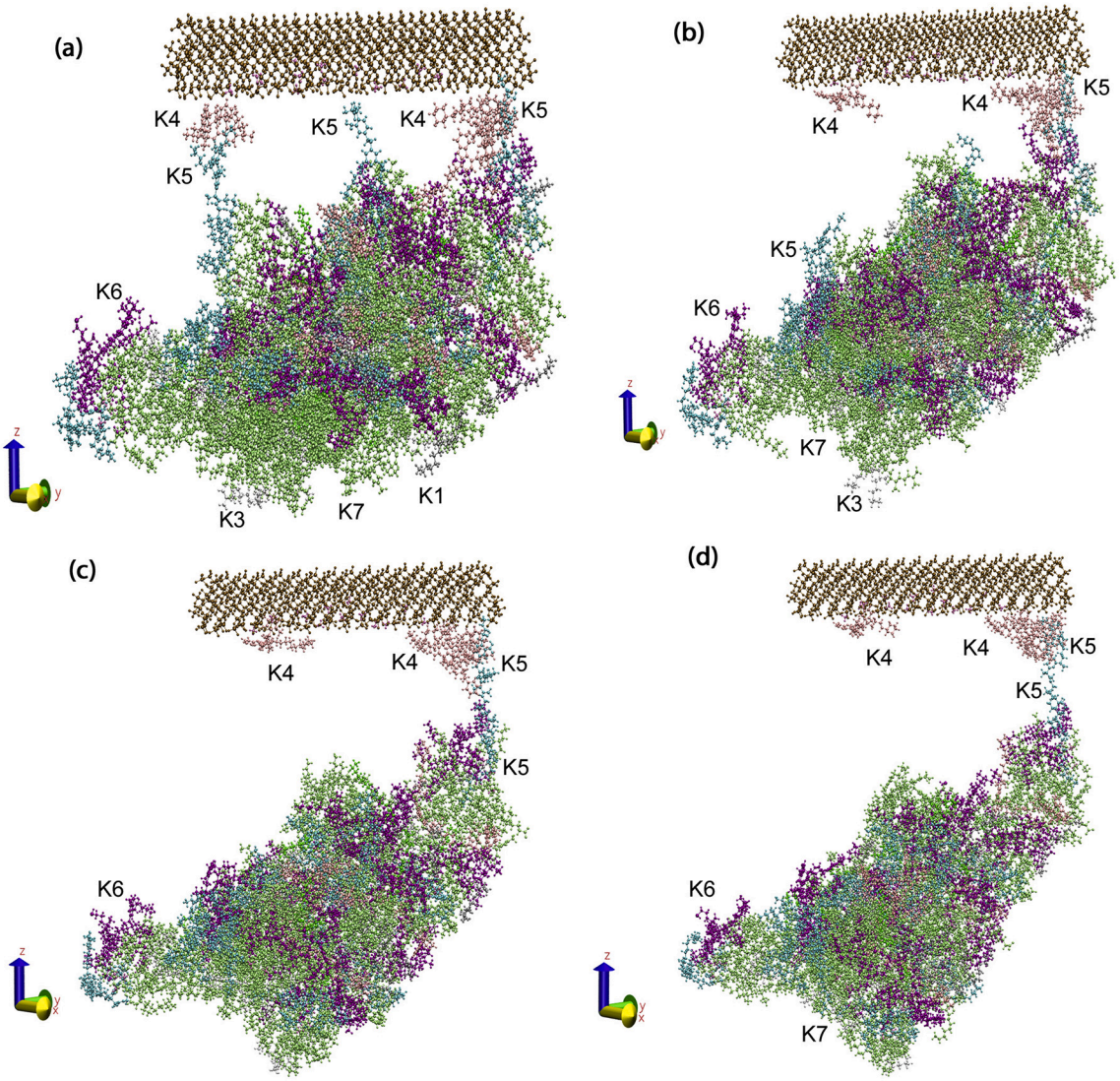

Fig. 5. The conformation of 'quartz supercell on top of kerogen' model at (a) 1 ns, (b) 2 ns, (c) 3 ns, and (d) 4 ns. All the representations were generated by VMD 1.9.3. Different colored segments represent different fragments of kerogen. Fragment 4 is pink colored, and fragment 5 is cyan colored. Kerogen fragments 1, 2, 3, 4, 5, 6, and 7 are represented by K1, K2, K3, K4, K5, K6, and K7, respectively. (For interpretation of the references to colour in this figure legend, the reader is referred to the web version of this article.)

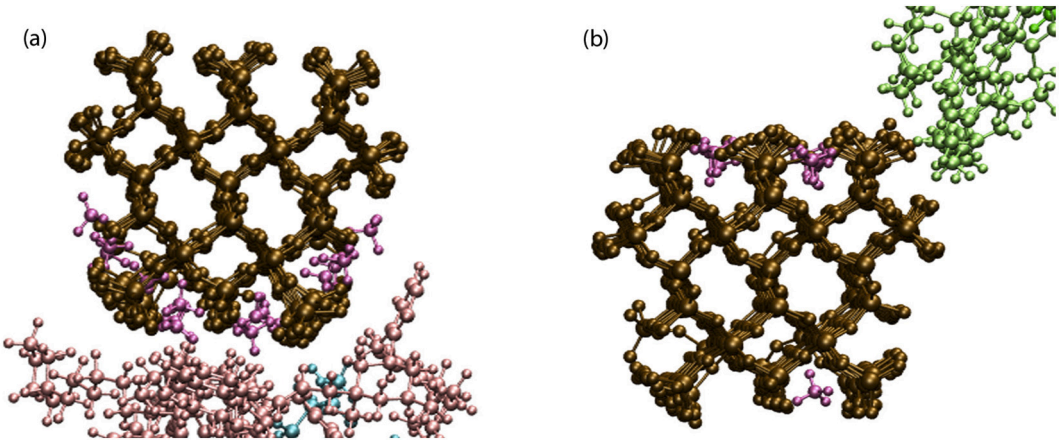

Fig. 6. A magnified view of stuffing sites (cavities) of quartz supercell providing accommodation to NH_4 ions in (a) quartz supercell on top of kerogen model and (b) quartz supercell at the bottom of kerogen model. The five-atomic mauve-colored segments are ammonium (NH_4) ions. (For interpretation of the references to colour in this figure legend, the reader is referred to the web version of this article.)

Table 2
Nonbonded interaction energies (kJ/mol) of quartz supercell with kerogen fragments with time in 'quartz supercell on top of kerogen' model.

Kerogen fragments	Total nonbonded energy (kJ/mol)			
	1 ns	2 ns	3 ns	4 ns
1	0	0	0	0
2	0	0	0	0
3	0	0	0	0
4	−602	−742	−756	−750
5	−858	−592	−450	−442
6	−2	−18	0	0
7	0	−10	0	0
8	−25,276	−27,665	−27,468	−27,486

are a result of the interaction between NH_4 groups and quartz.

The bar graph (Fig. 4b) shows that the total nonbonded energy between quartz supercell and 12-unit kerogen increased from −26,738 kJ/mol at 1 ns to −29,027 kJ/mol at 2 ns. The negative energy values indicate attractive interactions. Then it reached the equilibrium at 4 ns with the energy slightly decreasing to −28,678 kJ/mol. The plot also exhibits that attractive nonbonded interactions are mainly electrostatic. The nonbonded interactions occur only between the top chain (layer) of kerogen and quartz. The nonbonded energies between the top and bottom chain (layer) of kerogen were calculated both in the absence and presence of quartz supercell. In the absence of quartz, the nonbonded energy between the top and bottom chain (layer) was −2656 kJ/mol. However, as the quartz supercell was placed on the top of kerogen, the nonbonded energy between kerogen chains (layers) increased to −4862 kJ/mol at 1 ns, −5135 kJ/mol at 2 ns, −5372 kJ/mol at 3 ns and − 5356 kJ/mol at 4 ns of simulation. The merging of both chains and migration of some NH_4 groups from the top chain (layer) to bottom chain (layer) can be attributed to this increase of nonbonded energy.

3.2. Quartz supercell at the bottom of the kerogen model

Fig. 7a illustrates that the agglomeration of bonded, nonbonded, and kinetic energies of this model attains the equilibrium condition around 4 ns of simulation. Snapshots were taken at 1 ns increments to visualize the changes at various stages of the simulation (Fig. 8).

The beginning of the simulation at room temperature and pressure (300 K and 1.01325 bar) was marked by the rapid migration of 5 NH_4 groups from the bottom chain (layer) of kerogen to quartz supercell. All these NH_4 groups filled some of the stuffing sites of the supercell (Fig. 6b). Fragments 3 and 7 from the bottom chain of kerogen moved slightly towards the quartz. At the end of 1 ns, 5 more NH_4 groups from the bottom chain moved to the stuffing sites of quartz supercell. Fragments 2, 3 and 7 were interacting with the quartz supercell at this point

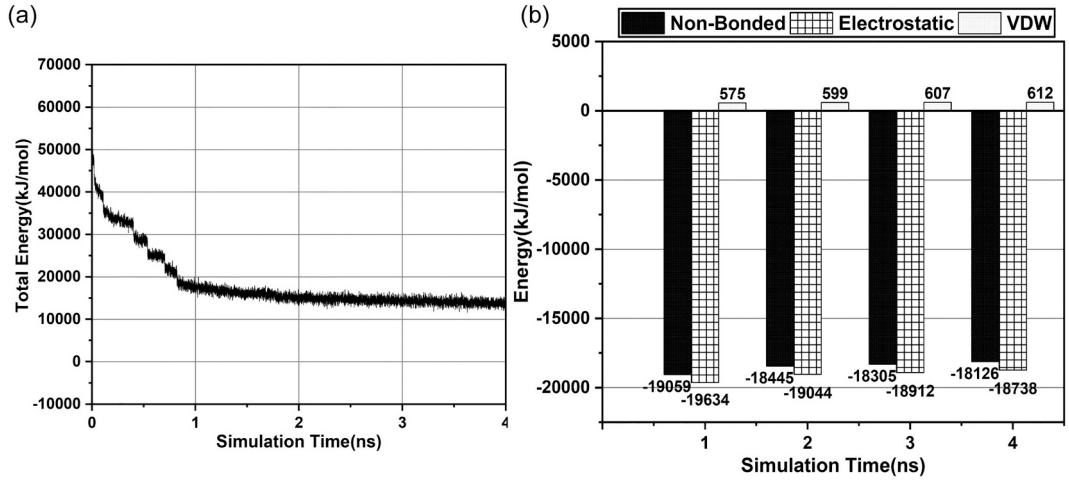

Fig. 7. (a) Total energy vs. time plot, and (b) bar graph showing nonbonded energy acting between quartz supercell and 12-unit kerogen with time for 'quartz supercell at the bottom of kerogen' model.

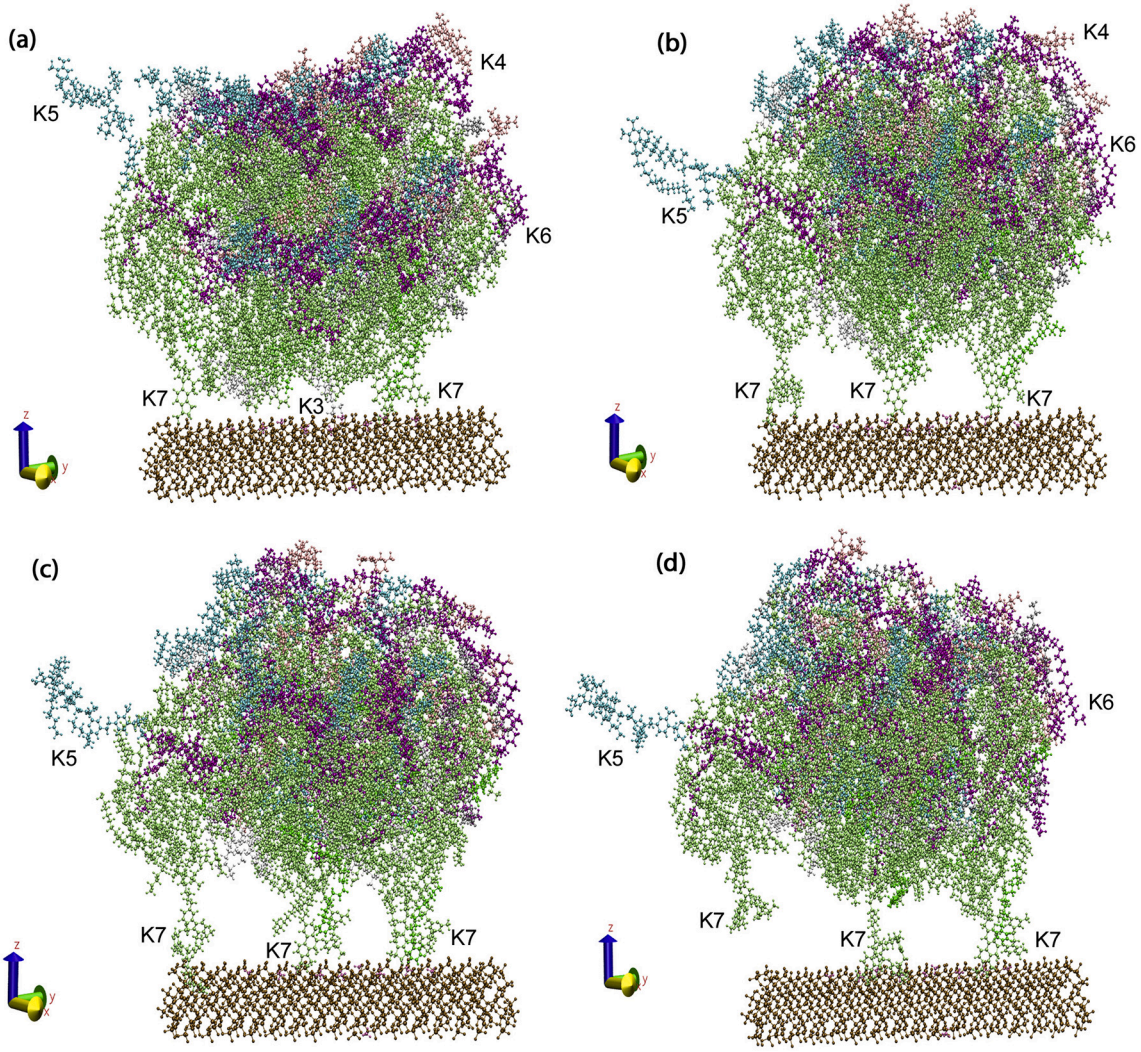

Fig. 8. The conformation of 'quartz supercell at the bottom of kerogen' model at (a) 1 ns, (b) 2 ns, (c) 3 ns, and (d) 4 ns. All the representations were generated by VMD 1.9.3. Different colored segments represent different fragments of kerogen. Fragments 3 and 7 are white and lime-colored, respectively. The 'mostly detached' fragment 5 is a cyan colored leftmost segment at 4 ns. Kerogen fragments 1, 2, 3, 4, 5, 6, and 7 are represented by K1, K2, K3, K4, K5, K6, and K7 respectively. (For interpretation of the references to colour in this figure legend, the reader is referred to the web version of this article.)

(Fig. 8a).

All these interacting fragments belonged to the bottom chain (layer) of kerogen. After simulation of 2 ns, all the fragments except fragment 7 moved away from the quartz supercell. Three segments of fragment 7 from the bottom chain (layer) were interacting with the supercell (Fig. 8b). As the simulation approached 3 ns, the interaction behavior remained similar to the one observed at 2 ns (Fig. 8c). At the end of 4 ns of simulation, only two segments of fragment 7 had interaction with the quartz supercell (Supplementary Fig. 17). A segment of fragment 5 from the bottom chain mostly detached from the rest of kerogen (Fig. 8d).

Table 3 implies that in this model, only fragments 7 and 8 had significant nonbonded interactions with quartz supercell. Fragments 2 and 3 had little interaction with supercell, which further diminished at 4 ns equilibrium condition.

Compared to the first model, NH_4 groups had 10,138 kJ/mol less nonbonded attractive interactions with quartz in this model. This phenomenon can arise from the difference in the number of NH_4 groups attached to the quartz supercell in the two models. In the first model, 14 NH_4 groups were attached to the supercell, while in the second model, 10 NH_4 groups were attached to the supercell.

The total nonbonded energy between quartz supercell and 12-unit kerogen decreased gradually with simulation time and reached equilibrium at 4 ns (Fig. 7b). The magnitude of nonbonded energy was −19,059 kJ/mol at 1 ns, −18,445 kJ/mol at 2 ns, −18,305 kJ/mol at 3 ns and −18,126 kJ/mol at 4 ns. The movement of kerogen fragments away from quartz supercell may be attributed to the observed decrease in the energy. Nonbonded interactions are mainly electrostatic similar to the first model. All the interactions took place between the bottom chain (layer) of kerogen and quartz. The nonbonded energy between the top and bottom chains (layers) of kerogen is also computed for this model.

Table 3
Nonbonded interaction energies (kJ/mol) of quartz supercell with kerogen fragments over time in 'quartz supercell at the bottom of kerogen' model.

Kerogen fragments	Total nonbonded interaction energy (kJ/mol)			
	1 ns	2 ns	3 ns	4 ns
1	−1	0	0	0
2	−73	−48	−45	−11
3	−66	0	0	0
4	0	0	0	0
5	0	0	0	0
6	0	0	0	0
7	−1542	−1026	−910	−767
8	−17,377	−17,371	−17,350	−17,348

The values are found to be −3100 kJ/mol at 1 ns, which slightly changed to −3175 kJ/mol at 4 ns. This observation implies that the presence of quartz supercell at the bottom of kerogen did not result in a large change in the inter-chain interaction of kerogen, as observed in the first model (quartz supercell on top of kerogen). In this model, instead of merging into each other, both chains (layers) remained side by side.

We have also investigated the inter-fragmental nonbonded energies inside kerogen for all three conditions (without quartz, quartz on top, and quartz at the bottom). Table 4 indicates that the presence of quartz caused changes in the interaction energies among the fragments of kerogen.

The attractive interactions of fragment 8 towards the fragments 6 and 7 were reduced when quartz was placed in the proximity of kerogen. The nonbonded energy between fragments 7 and 8 decreased from −57,129 kJ/mol (without quartz) to −42,703 kJ/mol (quartz on top) and −52,200 kJ/mol (quartz at the bottom). Nonbonded energy between fragments 6 and 8 decreased from −19,795 kJ/mol (without quartz) to −18,314 kJ/mol (quartz on top) and −17,879 kJ/mol (quartz at the bottom). Repulsive interactions between fragments 5 and 6 increased from 364 kJ/mol (without quartz) to 1548 kJ/mol (quartz on top) and 673 kJ/mol (quartz at the bottom). The interactions between fragments 5 and 7 became more repulsive with the presence of quartz (2129 kJ/mol in the absence of quartz, 2493 kJ/mol for quartz on top and 2393 kJ/mol for quartz at the bottom condition).

From the above analysis, it is evident that only the adjacent chain of kerogen interacted with quartz mineral in both orientations because the kerogen chains farther away from the quartz surface will have very small or infinitesimal interaction energy values with quartz. Among the eight fragments of kerogen, fragments 4, 5, 7, and 8 (NH_4 group) interacted significantly with quartz supercell. Fragments 4, 5, and 7 contain aromatic hydrocarbon rings (Supplementary Fig. 19). During the interaction, these hydrocarbon rings were attracted to the quartz. The hydrogen atoms of hydrocarbons were directed towards the oxygen atoms of quartz. The rapid movement of NH_4 groups to the quartz supercell is likely caused by their low molecular weight and higher electrostatic interactions with the supercell. Fragments 5, 7, and 8 contain nitrogen atoms in their structure. Fragment 5 contains 4 nitrogen atoms while fragment 7 contains 10 nitrogen atoms. These nitrogen atoms of fragment 5 and 7 are either aliphatic or aromatic in nature. The non-interacting fragment 6 contains only 1 nitrogen atom which is aliphatic. Therefore, it can be hypothesized that aromatic nitrogen content contributes for the interactions of fragment 5 and 7 with quartz mineral. It proved the hypothesis that one of the major binding interactions in the kerogen-mineral matrix occurs between nitrogen-containing organics and silicate minerals (Siskin et al., 1987). Previous modeling study also exhibited that kerogen moieties with nitrogen-content have significant nonbonded interactions with phyllosilicate clay minerals (Katti et al., 2014). This study identifies the dominant interactions between nitrogen-containing fragments of bulk kerogen model and quartz mineral qualitatively as well as quantitatively. Our observations of MD simulations differ with the observations found by quantum chemical (QM) calculations (Hantal et al., 2014). These deviations may arise from the differences in the types of shales and kerogens used. On top of that, we did not consider the presence of water on the silica surface, unlike the QM calculations. It is observed that the different initial model can result in different interaction energy magnitudes for the kerogen-quartz system, however, the relative contributions made by the fragments remains similar. (Supplementary Fig, 10, 11 and supplementary Table 1).

In summary, this is the very first study that models the molecular level interactions of macromolecular type-I kerogen found in Green River Oil Shale with quartz mineral. This study reveals which kerogen fragments primarily interact with quartz mineral, the reasons behind interactions and the relative strength of their interactions. This study also shows how the ammonium ions occupy the quartz cavities indicating their strong affinities towards silicate minerals. These models could serve as in silico testbeds to screen new methodologies for efficient extraction of kerogen from the oil shale mineral matrix.

Table 4
Nonbonded interaction energies between kerogen fragments in three different conditions.

Interacting kerogen fragments	Total nonbonded energy (kJ/mol)		
	Kerogen only	Quartz on top of kerogen	Quartz at the bottom of kerogen
5-6	364	1548	673
5-7	2129	2493	2393
5-8	−13,222	−13,628	−11,972
6-7	3870	3630	3986
6-8	−19,795	−18,314	−17,879
7-8	−57,129	−42,703	−52,200

4. Conclusions

In the current study, we have performed molecular dynamics (MD) simulations on two different arrangements of quartz supercell and 12-unit kerogen model of Green River oil shale. We primarily studied the nonbonded interactions between different fragments of kerogen and α-quartz. We have also explained the conformations of both models at room temperature and pressure. Our findings can be summarized as:

1. The interaction between quartz supercell and 12-unit kerogen is initial-orientation specific. The initial arrangement dictates the amount of nonbonded energy between the mineral and organic constituents.
2. Quartz-kerogen interplay is fragment specific. Only the fragments (4, 5, and 7) with a higher number of aromatic hydrocarbons and Nitrogen elements significantly interact with quartz.
3. The most significant interaction occurs between fragment 8 (NH_4 groups) and quartz. For both models, as soon as the simulation begins, the NH_4 groups from adjacent kerogen chain (layer) migrate into the stuffing sites of the quartz supercell.
4. Nonbonded interactions between kerogen and quartz mineral are predominantly electrostatic.
5. Inter-fragment interaction energies inside kerogen vary depending upon the presence and location of quartz mineral.
6. The presence of quartz mineral significantly affects the inter-chain (inter-layer) energy within the kerogen. This behavior also depends upon the location of the quartz supercell with respect to the kerogen.

Declaration of Competing Interest

On behalf of all authors, the corresponding author states that there is no conflict of interest.

Acknowledgments

The authors would like to acknowledge the financial support from the US Department of Transportation Mountain-Plains Consortium (MPC) Grant #: DTRT13-G-UTC38. We also recognize the computational facilities provided by North Dakota State University Computationally Assisted Science and Technology (CCAST) and NSF MRI grant #1229316 and # #2019077.

Appendix A. Supplementary data

Supplementary data to this article can be found online at https://doi.org/10.1016/j.coal.2021.103729.

References

Aboulkas, A., El Harfi, K., 2008. Study of the kinetics and mechanisms of thermal decomposition of moroccan Tarfaya oil shale and its kerogen. Oil Shale 25, 426–443.

Aboulkas, A., El Harfi, K., 2009. Effects of acid treatments on Moroccan Tarfaya oil shale and pyrolysis of oil shale and their kerogen. J. Fuel Chem. Technol. 37, 659–667.

Alstadt, K.N., Katti, D.R., Katti, K.S., 2012. An in situ FTIR step-scan photoacoustic investigation of kerogen and minerals in oil shale. Spectrochim. Acta A 89, 105–113.

Alstadt, K.N., Katti, K.S., Katti, D.R., 2016. Nanoscale morphology of kerogen and in situ nanomechanical properties of Green River oil shale. J. Nanomech. Micromech. 6.

Antao, S.M., Hassan, I., Wang, J., Lee, P.L., Toby, B.H., 2008. State-of-the-art high-resolution powder X-ray diffraction (HRPXRD) illustrated with Rietveld structure refinement of quartz, sodalite, tremolite, and meionite. Can. Mineral. 46, 1501–1509.

Ballice, L., 2005. Effect of demineralization on yield and composition of the volatile products evolved from temperature-programmed pyrolysis of Beypazari (Turkey) Oil Shale. Fuel Process. Technol. 86, 673–690.

Ballice, L., 2006. Stepwise chemical demineralization of Göynük (Turkey) oil shale and pyrolysis of demineralization products. Ind. Eng. Chem. Res. 45, 906–912.

Bhowmik, R., Katti, K.S., Katti, D.R., 2009a. Mechanisms of load-deformation behavior of molecular collagen in hydroxyapatite-tropocollagen molecular system: steered molecular dynamics study. J. Eng. Mech. 135, 413–421.

Bhowmik, R., Katti, K.S., Katti, D.R., 2009b. Molecular interactions of degradable and non-degradable polymers with hydroxyapatite influence mechanics of polymer-hydroxyapatite nanocomposite biomaterials. Int. J. Nanotechnol. 6, 511–529.

Borrego, A.G., Prado, J.G., Fuente, E., Guillen, M.D., Blanco, C.G., 2000. Pyrolytic behaviour of Spanish oil shales and their kerogens. J. Anal. Appl. Pyrolysis 56, 1–21.

Cane, R.F., 1976. In: Yen, T.F., Chilingarian, G.V. (Eds.), In Oil Shale. Elsevier, Amsterdam.

Chang, Z., Chu, M., Zhang, C., Bai, S., Lin, H., Ma, L., 2017. Compositional and structural variations of bitumen and its interactions with mineral matters during Huadian oil shale pyrolysis. Korean J. Chem. Eng. 34, 3111–3118.

Deng, S., Wang, Z., Gu, Q., Meng, F., Li, J., Wang, H., 2011. Extracting hydrocarbons from Huadian oil shale by sub-critical water. Fuel Process. Technol. 92, 1062–1067.

Eglinton, T.I., Rowland, S.J., Curtis, C.D., Douglas, A.G., 1986. Kerogen mineral reactions at raised temperatures in the presence of water. Org. Geochem. 10, 1041–1052.

Emami, F.S., Puddu, V., Berry, R.J., Varshney, V., Patwardhan, S.V., Perry, C.C., Heinz, H., 2014. Force field and a surface model database for silica to simulate interfacial properties in atomic resolution. Chem. Mater. 26, 2647–2658.

Faisal, H.M.N., Katti, K.S., Katti, D.R., 2020. Modeling the behavior of organic kerogen in the proximity of calcite mineral by molecular dynamics simulations. Energy & Fuels 34, 2849–2860.

Faisal, H.M.N., Katti, K.S., Katti, D.R., 2021. Molecular mechanics of the swelling clay tactoid under compression, tension and shear. Appl. Clay Sci. 200, 105908.

Forsman, J.P., Hunt, J.M., 1958. Insoluble organic matter (kerogen) in sedimentary rocks. Geochim. Cosmochim. Acta 15, 170–182.

Ghosh, P., Katti, D.R., Katti, K.S., 2007. Mineral proximity influences mechanical response of proteins in biological mineral-protein hybrid systems. Biomacromolecules 8, 851–856.

Guo, H., Lin, J., Yang, Y., Liu, Y., 2014. Effect of minerals on the self-heating retorting of oil shale: self-heating effect and shale-oil production. Fuel 118, 186–193.

Hantal, G., Brochard, L., Cordeiro, M., Ulm, F.J., Pellenq, R.J.M., 2014. Surface chemistry and atomic-scale reconstruction of kerogen-silica composites. J. Phys. Chem. C 118, 2429–2438.

Ikuta, D., Kawame, N., Banno, S., Hirajima, T., Ito, K., Rakovan, J.F., Downs, R.T., Tamada, O., 2007. First in situ X-ray identification of coesite and retrograde quartz on a glass thin section of an ultrahigh-pressure metamorphic rock and their crystal structure details. Am. Mineral. 92, 57–63.

Jain, S.K., Pellenq, R.J.M., Pikunic, J.P., Gubbins, K.E., 2006. Molecular modeling of porous carbons using the hybrid reverse Monte Carlo method. Langmuir 22, 9942–9948.

Karabakan, A., Yurum, Y., 1998. Effect of the mineral matrix in the reactions of oil shales: 1. Pyrolysis reactions of Turkish Goynuk and US Green River oil shales. Fuel 77, 1303–1309.

Katti, D.R., Upadhyay, H.B., Katti, K.S., 2014. Molecular interactions of kerogen moieties with Na-montmorillonite: an experimental and modeling study. Fuel 130, 34–45.

Katti, D.R., Thapa, K.B., Katti, K.S., 2017. Modeling molecular interactions of sodium montmorillonite clay with 3D kerogen models. Fuel 199, 641–652.

Kelemen, S.R., Siskin, M., 2004. Organic Matter Models of Oil Shale Revisited, 49. Preprints-American Chemical Society. Division of Petroleum Chemistry, pp. 73–76.

Le Page, Y., Donnay, G., 1976. Refinement of the crystal structure of low-quartz. Acta Crystallogr. Sec. B 32, 2456–2459.

Liu, Q., Hou, Y., Wu, W., Wang, Y., Wang, Q., Ren, S., 2019. New insights into the occurrence and interaction of inorganic minerals and organic matter in Huadian Oil Shale. Energy Fuel 33, 859–867.

Luong, D., Sephton, M.A., Watson, J.S., 2015. Subcritical water extraction of organic matter from sedimentary rocks. Anal. Chim. Acta 879, 48–57.

Orendt, A.M., Pimienta, I.S.O., Badu, S.R., Solum, M.S., Pugmire, R.J., Facelli, J.C., Locke, D.R., Chapman, K.W., Chupas, P.J., Winans, R.E., 2013. Three-dimensional structure of the Siskin Green River oil shale kerogen model: a comparison between calculated and observed properties. Energy Fuel 27, 702–710.

Pan, L., Dai, F., Huang, P., Liu, S., Li, G., 2016. Study of the effect of mineral matters on the thermal decomposition of Jimsar oil shale using TG-MS. Thermochim. Acta 627, 31–38.

Payne, M.C., Teter, M.P., Allan, D.C., Arias, T.A., Joannopoulos, J.D., 1992. Iterative minimization techniques for abinitio total-energy calculations - molecular-dynamics and conjugate gradients. Rev. Mod. Phys. 64, 1045–1097.

Phillips, J.C., Braun, R., Wang, W., Gumbart, J., Tajkhorshid, E., Villa, E., Chipot, C., Skeel, R.D., Kale, L., Schulten, K., 2005. Scalable molecular dynamics with NAMD. J. Comput. Chem. 26, 1781–1802.

Pikunic, J., Clinard, C., Cohaut, N., Gubbins, K.E., Guet, J.M., Pellenq, R.J.M., Rannou, I., Rouzaud, J.N., 2003. Structural modeling of porous carbons: constrained reverse Monte Carlo method. Langmuir 19, 8565–8582.

Razvigorova, M., Budinova, T., Tsyntsarski, B., Petrova, B., Ekinci, E., Atakul, H., 2008. The composition of acids in bitumen and in products from saponification of kerogen: Investigation of their role as connecting kerogen and mineral matrix. Int. J. Coal Geol. 76, 243–249.

Saxby, J.D., 1970. Isolation of kerogen in sediments by chemical methods. Chem. Geol. 6, 173–184.

Sert, M., Ballice, L., Yuksel, M., Saglam, M., 2009. Effect of mineral matter on product yield and composition at isothermal pyrolysis of turkish oil shales. Oil Shale 26, 463–474.

Sikdar, D., Katti, K.S., Katti, D.R., 2008. Molecular interactions alter clay and polymer structure in polymer clay nanocomposites. J. Nanosci. Nanotechnol. 8, 1638–1657.

Siskin, M., Brons, G., Payack, J.F., 1987. Disruption of kerogen mineral interactions in oil shales. Energy Fuel 1, 248–252.

Siskin, M., Scouten, C.G., Rose, K.D., Aczel, T., Colgrove, S.G., Pabst, R.E., 1995. Detailed Structural Characterization of the Organic Material in Rundle Ramsay Crossing and Green River Oil Shales, Composition, Geochemistry and Conversion of Oil Shales. Springer, pp. 143–158.

Skelton, A.A., Fenter, P., Kubicki, J.D., Wesolowski, D.J., Cummings, P.T., 2011. Simulations of the Quartz(10(1)over-bar1)/water interface: a comparison of classical force fields, ab initio molecular dynamics, and X-ray reflectivity experiments. J. Phys. Chem. C 115, 2076–2088.

Stankiewicz, B.A., Kruge, M.A., Mastalerz, M., Salmon, G.L., 1996. Geochemistry of the alginite and amorphous organic matter from Type II-S kerogens. Org. Geochem. 24, 495–509.

Suleimenova, A., Bake, K.D., Ozkan, A., Valenza Ii, J.J., Kleinberg, R.L., Burnham, A.K., Ferralis, N., Pomerantz, A.E., 2014. Acid demineralization with critical point drying: a method for kerogen isolation that preserves microstructure. Fuel 135, 492–497.

Taskforce on Strategic Unconventional Fuels, 2007. America's Strategic Unconventional Fuels. US Government, Washington (DC).

Vandenbroucke, M., Largeau, C., 2007. Kerogen origin, evolution and structure. Org. Geochem. 38, 719–833.

Vanommeslaeghe, K., Hatcher, E., Acharya, C., Kundu, S., Zhong, S., Shim, J., Darian, E., Guvench, O., Lopes, P., Vorobyov, I., MacKerell, A.D., 2010. CHARMM general force field: a force field for drug-like molecules compatible with the CHARMM All-atom additive biological force fields. J. Comput. Chem. 31, 671–690.

Yan, J., Jiang, X., Han, X., Liu, J., 2013. A TG-FTIR investigation to the catalytic effect of mineral matrix in oil shale on the pyrolysis and combustion of kerogen. Fuel 104, 307–317.

Zhang, Z., Liu, H., Wang, J., 2020. Energetics of interfacial interactions of hydrocarbon fluids with kerogen and calcite using molecular modeling. Energy Fuel 34, 4251–4259.